Optical identifications of faint ultra-steep spectrum radio sources

Wieringa, M.H.; Katgert, P.

ASTRONOMY & ASTROPHYSICS
SUPPLEMENT SERIES

Astron. Astrophys. Suppl. Ser. **93,** 399-418 (1992)

Optical identifications of faint ultra-steep spectrum radio sources

M.H. Wieringa* and P. Katgert

Sterrewacht Leiden, P.O. Box 9513, 2300 RA Leiden, The Netherlands

Received August 22; accepted August 27, 1991

Abstract. — We present the first results of an observational study of ultra-steep spectrum sources selected on the basis of Westerbork surveys at 327 MHz complemented by observations at 608 MHz. The sample, with a spectral index > 1.1, is ~ 25 times fainter than the 4C-sample of USS sources first studied by Tielens *et al.* (1979) and currently by Chambers, Miley and van Breugel (1987). Here we describe high-resolution follow-up observations with the VLA, deep optical imaging ($R_{\rm lim} \sim 23.7$) and some spectroscopy. Elsewhere we discuss the implications of our observations. The decrease of the identification fraction with steepening spectral indexed observed in the 4C sample is also present in our faint source sample. We find no evidence for alignment between the optical and radio axes, and have not found any strong emission lines in a subsample for which we obtained low-resolution spectroscopy.

Key words: Galaxies: radio – Galaxies: formation of.

1. Introduction.

The use of ultra-steep spectrum (USS) radio sources to probe the distant universe has flourished since the findings of Tielens *et al.* (1979) and Blumenthal and Miley (1979) that there is a correlation between the identification fraction on the Palomar Sky Survey and the radio spectral index for flux-limited radio samples. It was found that the identification fraction dropped considerably for sources with very steep spectra, which suggests that these sources have very faint identifications beyond the plate limit, most likely with distant galaxies (Blumenthal and Miley, 1980) The correlation found by Tielens *et al.* allows a purely radio-based selection of galaxies that have a high probability of being very distant. Chambers, Miley and van Breugel (1987) and Chambers (1989) used this method to study a sample of 33 4C sources with steep ($\alpha > 1$ for $S_\nu \propto \nu^{-\alpha}$) radio spectra over the range 178–5000 MHz. The method has proven its value, because of the 33 sources selected, 50% are at $z > 0.5$ and half of these even at $z > 2$. The most distant galaxy found to date is 4C41.17 at $z = 3.8$ (Chambers *et al.*, 1990).

There are several multi-spectral projects currently underway at Leiden to exploit the USS source selection technique to study distant radio galaxies. Röttgering, Chambers and Miley together with several external collaborators (Miley et al., 1989) are extending the studies of bright USS sources over the whole sky and to slightly fainter flux densities (factor ~ 3) than the 4C sample. Here we present the results of a project which uses 327 MHz (92 cm) Westerbork observations of six fields, in combination with 608 MHz (49 cm) observations, to extend the sample of USS sources to sources about 25 times fainter than the 4C sample. We have confined our study to the smaller USS sources ($< 25''$) since they are more likely to be distant (e.g., Barthel and Miley, 1988)

2. Radio observations: reduction and calibration.

In 1985 a project was started to search for the redshifted 21 cm line of high redshift neutral hydrogen and to study the radio continuum sky using the then newly available 327 MHz receivers at Westerbork (Wieringa, 1991). We observed six fields at 327 MHz, for part of which 608 MHz observations were either already available or were obtained later. Wieringa (1991) summarizes the available low frequency data. We selected a sample of USS sources ($\alpha_{49}^{92} > 1.1$) from these fields, which we subsequently observed using the VLA at 20 cm. The VLA observations were done in snapshot mode, partly in C- and partly in A-configuration.

Send offprint requests to: P. Katgert.
* Present address: CSIRO, Australia Telescope National Facility, Paul Wild Observatory, PO Box 94, Narrabri NSW 2390, Australia.

2.1. The 327 and 608 MHz Westerbork data.

We describe the 327 and 608 MHz observations in more detail elsewhere (Wieringa, 1991), here we give a brief overview of the procedures followed. All Westerbork observations were reduced using a set of programs, written by W.N. Brouw, and running in the DWARF system, which makes use of the redundant baselines in the Westerbork array to determine model independent telescope corrections (Noordam and de Bruyn, 1982; Wieringa, 1991).

After interference removal based on displays of the uncorrected amplitudes, we applied redundant baseline calibration to correct telescope based errors. Depending on the array configuration only 2–4 parameters need to be determined after this calibration step per scan (solution time interval). These remaining parameters, which represent overall flux and position and possibly some additional phase slopes, were determined iteratively, using a model of the sky brightness distribution as input to the alignment program in DWARF. This program ties all internally consistent scans to the average flux and position scale of the observation. Thereafter the maps were cleaned and the components restored with a gaussian beam (fitted to the central part of the synthesized antenna pattern).

Calibration sources were observed directly before and after the observations. The absolute flux scale was calibrated assuming a flux of 26.93 at 327 MHz and 21.47 at 608 MHz for 3C286, which served as the primary flux calibrator. We estimate the flux scales to be correct to within $\sim 5\%$. There may be larger flux scale differences with the 608 MHz fields observed earlier: Lynx (Windhorst, 1984), and UMi (Katgert-Merkelijn *et al.*, 1985); for the UMi field we have multiplied the 608 MHz fluxes by 1.12 before calculating spectral indices. This correction factor was determined using our 327 MHz fluxes and the 1420 MHz fluxes for the UMi field presented by Katgert-Merkelijn *et al.*, such that it makes the individual radio spectra of the sources detected at all three frequencies straight on average.

The position frames of the fields were calibrated relative to each other using overlap regions and then calibrated absolutely using one or more identified strong point sources with accurate radio or optical positions. Corrections applied were in the range of 1 to 5″; we expect that no systematic errors much larger than 2″ remain.

Sources in the final maps which had a peak intensity exceeding 5 times the noise level, were fitted with a two dimensional gaussian brightness distributions to determine total flux densities, positions and an indication of their angular sizes. The flux densities of the most extended sources were determined by summing the pixel intensities over the source (and dividing by the summed intensities of the synthesized beam).

2.2. The VLA observations.

On June 3 and 4 1989 we observed a sample of 50 compact USS sources ($S_{92} > 50$ mJy, size$< 25''$ at 327 or 608 MHz) with the VLA. The observations were made with the C-array (giving a synthesized beam of about 12″) at 1490 MHz with 2×50 MHz bandwidth. The sources were observed for about 8–9 minutes each, split in two parts about 2 hours apart, to improve the u-v-coverage.

The system phase and amplitude gain were calibrated using nearby standard VLA calibrators observed about every half hour. These measurements were tied to the primary flux calibrator 3C286, observed once on both days.

The visibility data were reduced using AIPS on a Convex at the Array Operations Center of NRAO in Socorro. First, we flagged regions of interference using the task TVFLG. Raw-amplitude and rms-amplitude displays were used to locate the interference. Absolute calibration was carried out using the CALIB program. Because our sources were located in five areas (containing the six 92 cm fields), we used a separate calibrator near each area to determine the time-interpolated corrections for each source. After combining data from the two frequency bands the calibrated visibility data were Fourier transformed and cleaned using the MX program. Sidelobes of distant sources, if present, were removed using multiple fields cleaned simultaneously. Effects of interference were further reduced by clipping the residual visibility data after subtraction of the model at 4–5 times the noise level and remapping the fields. No selfcalibration was performed, because the intensities of most sources were smaller than 100σ and no large defects were visible in the maps.

On April 3 and 6 1990 we observed 61 USS sources using the VLA in the A-configuration. For 20 of these sources C-array observations had already been obtained, but because of complex radio structure and/or an uncertain optical identification, higher resolution data were needed. The remaining sources represent an extension of the sample of USS sources to slightly lower 327 MHz flux densities (> 30 mJy). Observations were made at 1490 MHz with 2×50 MHz bandwidth. We observed each source for 12–14 minutes, again split in two parts. Nearby calibrators were observed every 30 minutes. The primary flux calibrator 3C286 was observed on both days, but the second observation of 3C286 was lost due to on-line computer problems.

The 1990 observations were carried out in absentee observing mode. Calibration and mapping were done in Leiden using AIPS on a combination of a Convex mini-supercomputer and a Sun workstation. The procedure followed was identical to that used for the C-configuration data. We determined the absolute flux scale of the observations of the second day by comparing the secondary calibrators observed on both days. For the first day these

were tied to 3C286. This allowed us to bring all data to the same flux scale. Due to the much higher resolution ($\sim 1.2''$) of the A configuration maps, several sources were sufficiently resolved out that estimation of their flux densities was difficult. To alleviate this problem we also made $2''$-resolution maps and, if necessary, $4''$-resolution maps by application of a tapering function that emphasized the visibilities on the short baselines. A few sources were not detected in A-configuration, not even at $4''$-resolution.

Source parameters (flux densities, positions, sizes) were determined by gaussian fitting for unresolved or slightly resolved sources and sources with only compact components and by pixel summation and interactive estimates for more complex and larger sources. Most complex sources could be fitted easily in the lower resolution maps. We estimate the position errors for the C-configuration to be $\sim 0.5''$ and for the A-configuration $\lesssim 0.3''$. Flux scales are estimated to be correct within 5%, but for extended sources errors may be somewhat larger.

3. Optical imaging and spectroscopy.

We have attempted optical identification of a sub-sample of sources in four CCD imaging runs on the 2.5 m INT at La Palma, in May, August and December '89 and April '90. These runs were shared with Röttgering, Chambers and Miley who observed sources from their radio-bright sample of USS sources. We used the KPNO system R band filter ($\lambda = 646$ nm, $\Delta\lambda = 126$ nm) and the RCA chip. We observed each of the sources for a total of 30 minutes with two separate integrations of 15 minutes. We moved the telescope by about $10''$ between exposures to reduce the effects of single bad pixels and other chip defects ('black holes'). Because the CCD frames are sky limited, and because the positions of objects do not coincide between frames, a median through all frames (after bias subtraction and scaling to a median of one) gives a very accurate flat-field. The flat-fields produced in this way include effects due to global illumination, pixel to pixel sensitivity variations and interference fringing. The resulting flat-fielded images are free from the high spatial frequency fringes at a level of ~1% which are present in images flat-fielded with e.g., twilight or dome flat-fields. These fringes would otherwise limit the detection of faint objects. The resulting noise in 'empty' regions of the CCD frames approaches the theoretical value to within 10%.

Of course, the above procedure only works well if atmospheric conditions during the night are stable. In some cases we needed to divide the CCD frames in two or three groups for which separate median flat-fields were determined. In a few images obtained during nights which were largely cloudy some fringing remains present. The flat-fielding was done at La Palma using the standard FIGARO and STARLINK software, with some small modifications.

3.1. Flux and position calibration.

The CCD images were calibrated to an absolute flux scale using exposures of 2–3 different standard stars taken near the beginning, middle and end of the night. Standard star magnitudes were taken from Landolt (1983). Generally the magnitudes of the standard stars were consistent within a night to within 0.05 magnitude. No atmospheric or galactic extinction corrections were applied. We expect the derived magnitudes to be correct to about 0.2 magnitude (except for the faintest and largest objects).

The calibration of the CCD position frames was carried out in different ways for the various observing sessions. For the first session separate position frames were determined for the two 15 minute CCD exposures using lists of star positions determined from the Space Telescope Science Institute scanned plate archive (GASP) and corresponding local maximum fits on the CCD's. After application of the required transformation (using the AIPS program XTRAN) the images were added. For the subsequent observing sessions we first registered the two individual 15 minute exposures using cross-correlation to determine the relative shift. When precautions are taken not to include saturated pixels in the cross-correlation, the accuracy of this method is estimated to be better than 0.2 pixels ($0.15''$). We then determined the position frames for the combined images. For the second and third session the position frames were determined using measurements on POSS plates. We first derived a position reference frame on the basis of 10–15 bright stars and then measured the positions for a second set of 5–10 stars which were also visible on the CCD. Subsequent application of the transformation was similar to that of the first session. For the last session we obtained the STScI/GASP digitized plate regions corresponding to the CCD frames. We then fitted corresponding stars on plate and CCD frame using the NOAO/IRAF package and determined the α and δ of the stars from the plate solution. We then attached coordinate frames to the CCD frames using the XTRAN program.

The resulting positional accuracy is estimated to be about 0.8–$0.9''$ for the first session (consisting of $0.7''$ intrinsic accuracy of the STScI positions and $0.3''$ in the star positions on the CCD frames). We estimate a slightly lower accuracy for the sessions using POSS positions (0.9–$1.1''$). The positions for the last session are expected to be most accurate: 0.7–$0.9''$. For a few frames the positions errors may be slightly larger due to unevenly distributed stars or off-center objects.

3.2. Optical spectroscopy.

In January 1990 we obtained optical spectroscopy for a sample of 13 identified USS sources on the 4.2 m WHT on La Palma. We used the Faint Object Spectrograph and obtained two 30 minutes exposures of each object at ~35Å resolution ($2.5''$-slit), with a sampling of 8.73Å/pixel. The

wavelength range covered was 4900–9700Å. For all these objects we have detected the faint continuum emission, although sometimes only at very low signal-to-noise ratios (1–2). We have not found any strong emission lines in our objects, therefore we cannot determine their redshifts.

4. Radio sample selection and properties.

The selection criteria for the radio sources in our sample are: $S_{92} > 30$ mJy, $\alpha_{49}^{92} > 1.1$ and a size $\psi < 25''$ as determined from the low frequency data. Here S_{92} is the flux density at 327 MHz (92 cm) and α_{49}^{92} is the spectral index between 327 MHz and 608 MHz. The last criterion excludes very extended sources and diffuse sources which would be more difficult to observe at higher frequency/resolution. With these criteria the sample contains ~ 100 sources out of a total of 880 sources detected at both 327 (with $S_{92} > 30$ mJy) and 608 MHz. There is about an equal number of USS sources which is estimated to be larger than $25''$ on the basis of the low resolution maps.

Figure 1 is a plot of α_{20}^{92}, as determined from the VLA 20 cm data, against the selection spectral index α_{49}^{92}. For the majority of the sources the difference in spectral index is $\lesssim 0.15$, there are a few outliers on both sides. Some of these can be explained by either a very low S/N-ratio at 49 cm or missed flux at 20 cm. Figure 2 is a histogram of the 92 cm flux densities. The median flux of the sample at 92 cm is ~ 60 mJy.

The radio data are presented in Table 1 (first line of each entry) for the sources for which we have obtained CCD images and in Table 2 for those which have not been observed optically. For each source a weighted average spectral index was determined on the basis of the three flux density points. The tables are organized as follows:

Column 1: The standard name of the object, this corresponds to the name in the middle of the first line above each plot in Figure 3.

Column 2, 3: The B1950 right ascension and declination and its error.

Column 4: (marked 'pos. code') Indicates which observation was used for the radio position given (20A=VLA A-array, 20cm, 20C=VLA C-array 20cm, 49=49cm WSRT, 92=92cm WSRT)

Column 5–7: The fluxdensity and its error at 327, 608 and 1490 MHz.

Column 8: The weighted spectral index over the 327–1490 MHz range. An S or F after the spectral index indicates probable steepening or flattening of the spectrum towards higher frequency.

Column 9–11: The radio structure is indicated by a C for compact/unresolved sources, an E for extended sources, a D for doubles and a T for triples. It is followed by the major axis and the position angle.

Column 13: (=Col. 12 in Tab. 2) notes for the radio data: + for a steep spectrum source belonging to the sample, − for a source no longer in the sample because of its radio spectrum, * indicates a note to the table.

5. Optical identifications.

In Table 1 we give the optical identification candidate for each radio source on a second line if found. The organization of the table is as follows:

Column 2,3: The B1950 right ascension and declination

Column 10,11: The optical structure: major axis and position angle

Column 12: The optical magnitude in KPNO R-band

Column 13: The notes for optical data: + for a reliable or highly probable identification; − for an empty field, this indicates $R > 23.5$ unless noted otherwise below. An S added to the + sign indicates the identification is likely but not certain due to the complex radio structure, an F indicates very faint, but probably correct id.'s, and a P indicates probable identifications with a radio-optical position difference in the range 2–3″.

Four sources in the original sample turned out not to be USS sources (based on the 1490 MHz data), but this became known only after optical imaging had been obtained. These sources are included here for completeness but marked with a minus sign in the radio notes column. For all sources with a positive identification the corresponding object was visible in both of the individual CCD-frames, which indicates that our optical flux limit is slightly conservative, and that no id's were made with cosmic rays.

Because our radio data are not of uniform resolution (20 cm C-array and A-array mixed, for a few sources only 92 cm and 49 cm) it is difficult to define an objective criterion to accept or reject optical identification candidates. In a some cases the high resolution A-array structure gives a clear indication that the optical identification lies more than 2.5″ (~ 2 times the combined radio-optical position error) from the center of gravity of the source. We have therefore judged all candidates by eye, incorporating all available information to decide whether a given candidate was acceptable. Based on the object density on our CCD frames of about 1 object per 120 arcsec^2, we expect ~16% spurious identifications within a radius of 2.5″ (i.e., reliability ~84%). On the other hand the completeness of the identifications (searching to about two times the combined position error) is about 86%. In absolute numbers this means there will be about 7 spurious identifications and 3 missed identifications for the 46 objects for which identification was attempted (excluding 3 objects for which identification was impossible because of nearby stars). The magnitude distribution of optical objects in the range $R = 20$–24 (Tyson, 1988) shows an increase

in $\log(N)$ of 0.39 per magnitude. Taking the last two complete magnitude bins of the identified objects (21.5-22.5-23.5) we find an identical increase (from 5 to 13). Therefore the spurious identifications do not systematically change the magnitude distribution.

In Figure 3 we give all radio/optical overlay plots for the sources in the USS sample. The low frequency positions (92 and 49 cm) are indicated by crosses, with the sizes of the crosses indicating the 1σ-errors. The gray scale of the plots runs from -1σ to $+3\sigma$, where $\sigma = \sqrt{N}$ is the theoretical noise calculated from the median number of photons (N) due to sky per pixel. The conversion factor from ADU (used in the plots) to photons is 3.8.

6. Analysis.

Elsewhere (Wieringa & Katgert, 1991) we present a full discussion of our observations, here we investigate a number of statistical properties of our sample.

6.1. Magnitude distribution.

The magnitude distribution of the identified sources is shown in Figure 4a. The identification percentage of the 46 sources in the USS sample is 57%(±7%) including a few very faint objects. The 50% identification percentage is reached beyond the formal limit of $R = 23.7$. The virtual absence of identifications below $R = 22$ is striking in view of the fact that the magnitude distribution of a 100% identified faint radio source sample (Fig. 4b) shows a peak at $R \sim 21$ (Windhorst *et al.*, 1987).

6.2. Variations of the identification fraction with spectral index.

In Figure 5 we present the optical identification fraction as a function of radio spectral index. A decrease of the identification fraction with increasing spectral index is found. The effect is similar to that found by Tielens *et al.* (1979) for a sample of 4C-sources. They determined the identification fraction on POSS plates down to a limiting magnitude of 19.4 and found a strong decrease in the identification fraction for steepening spectral index. Note that our median radio flux is a factor of ~ 25 fainter than for the 4C objects and our magnitude limit is ~ 4.3 magnitudes fainter (factor 50). The canonical interpretation of the effect is that the USS sources are the most powerful in the sample and thus, at a given observed flux density, the most distant. The remarkable agreement of Figure 5 with the results for the 4C sources suggests that this correlation is still present at much lower radio luminosities.

6.3. The optical morphology.

Using a gaussian fitting procedure we have estimated the sizes of the objects identified and presented in Table 1. In Figure 6 we show the histogram of optical angular sizes. A considerable fraction of the sources is either unresolved (i.e, not convincingly larger than the stellar images which are determined by a seeing of 1.2–1.6″) or very small. For the objects with $R > 23$ the estimated sizes are very uncertain, but it is clear that the number of extended or multiple optical objects is very small. Caution must be exercised in drawing conclusions based on optical sizes. Selection effects play an important role: because most of our identifications are fairly close to the detection limit we may have systematically missed low surface brightness objects.

6.4. Radio optical position angle differences.

One of the most striking differences between the radio-bright sample and our radio-faint one is the absence of a significant correlation between the radio and optical position angles of the identified sources. When we limit the sample to objects clearly resolved both in radio and optically ($\psi > 3''$), the histogram of position angle differences (Fig. 7) shows no evidence for alignment. This contrasts with results for the 4C sample (Chambers *et al.*, 1987) and the 3C sample (McCarthy *et al.*, 1987) for which there is a strong correlation (for the high redshift objects).

6.5. The optical spectra.

The absence of strong emission lines in the spectra of our USS sources indicates that the sources are likely to have optical spectra that are systematically different from those of the galaxies in the 3C, 4C and Texas sample, many of which have strong optical emission lines. We estimate that we have reached a sensitivity similar to that in the other samples, which were obtained on other telescopes. However, because our objects are, on average, somewhat fainter than those in the two other samples, it is possible that emission lines will appear in exposures reaching effectively ~ 1 magnitude deeper.

A more thorough analysis is needed to compare the equivalent width of emission lines between the various samples and to allow quantitative conclusions about them to be drawn.

7. Conclusions.

In this section we draw preliminary conclusions on the basis of the information available to date. A more detailed comparison will only be possible after the detailed statistics for the 4C and Texas samples become available.

A comparison of the magnitude distribution of our USS sources with the deep radio-optical sample of Windhorst *et al.* (1987) shows that the magnitude at which an identification fraction of 50% is reached, is $\sim$ 2 magnitudes fainter for the USS sample ($R \sim 24$ and $R \sim 22$). The radio fluxes of the Windhorst sample are $\sim$ 5–10 times lower, but various studies (e.g., Windhorst, 1984) have shown that the redshift distribution of radio source samples with $S_{20} < 100$ mJy probably does not change significantly with radio flux limit.

It is therefore unlikely that most of the USS sources are at redshifts similar to normal radio galaxies ($z < 1$). It suggests that even at flux densities below $\sim$ 100 mJy (at 327 MHz) a selection on steep spectrum (and small size) still preferentially selects the optically faintest and thus probably most distant radio sources. These sources would then have systematically higher radio power than average.

A clear indication that we are selecting on redshift is given by the drop in the identification percentage with increasing spectral index (Fig. 5). If confirmed with a larger sample this would indicate that the steep spectrum-redshift correlation is present over at least two decades in radio flux density. The fact that the fraction of USS sources $\alpha > 1.1$ at 327 MHz of $\sim$ 20–25% (for $S_{92} > 30$ mJy) is certainly not lower than for the 4C sample implies that the radio spectrum is correlated primarily with redshift rather than with power. This is consistent with the findings of Katgert-Merkelijn *et al.* (1980). Such a spectral index-redshift correlation could be due to environmental effects, i.e., a higher intergalactic density. Another possibility is that we are selecting similar sources in a different phase. Spectral curvature combined with the redshift provides an alternative explanation (Kapahi & Kulkarni, 1990) for which neither evolution nor redshift dependent effects are needed.

Here we have given only a preliminary analysis of the properties of the faint source USS sample. A more detailed investigation awaits completion of the data analysis of the various brighter USS samples being studied at Leiden. Careful and uniform comparisons of these samples should yield important information about the luminosity function of USS galaxies and the evolution of these properties with redshift. Further optical spectroscopy and IR imaging of our faint source sample would be useful in this regard.

Acknowledgements.

We thank Ken Chambers and Huub Röttgering for providing us with the STScI star positions and plots for our first imaging run and Eline Tolstoy for providing us with STScI/GASP scanned plate regions for our last run. We also thank the staffs at the VLA, the WSRT and La Palma for their assistance with the observations. We thank George Miley for a critical reading of a previous version of this paper. NRAO is operated by Associated Universities Inc., under contract with the National Science Foundation. The Westerbork Synthesis Radio Telescope is operated by the Netherlands Foundation for Research in Astronomy (NFRA) with financial support from the Netherlands Organization for scientific research (NWO). The Isaac Newton Group of Telescopes at the Observatorio del Roque de los Muchachos del Instituto de Astrofisica de Canarias is operated by the Royal Greenwich Observatory on behalf of the Science and Engineering Research Council (UK) and the Nederlandse organisatie voor wetenschappelijk onderzoek (NL).

References

Barthel P.D., Miley G.K. 1988, Nat 333, 319
Blumenthal G., Miley G.K. 1979, A&A 80, 13
Chambers K.C. 1989, Ph.D. Thesis, The Johns Hopkins University
Chambers K.C., Miley G.K., van Breugel W. 1987, Nat 329, 604
Chambers K.C., Miley G.K., and Joyce R.R. 1988, ApJ 329, L75
Chambers K.C., Miley G.K. 1989, in 'The Evolution of the Universe of Galaxies', The Edwin Hubble Centennial Symposium, R.G. Kron Ed. (ASP Conf. Ser., 10)
Chambers K.C., Miley G.K., van Breugel W.J.M. 1990, ApJ 363, 21
Kapahi V.K., Kulkarni V.K. 1990, AJ 99, 1397
Katgert-Merkelijn J., Lari C., Padrielli L. 1980, A&AS 40, 91
Katgert-Merkelijn, J., Robertson J.G, Windhorst R.A., Katgert P. 1985, A&AS 61, 517
Landolt A.U. 1983, A.J. 88, 439
McCarthy P.J., van Breugel W., Spinrad H., Djorgovski S. 1987, ApJ 321, L29
Miley G.K., Chambers K.C., Hunstead R., Macchetto F, Roland J., Röttgering H., Schilizzi R. 1989, ESO Messenger 56, 16
Oort M.J.A, Katgert P., Windhorst R.A. 1987, Nat 326, 500
Tielens A.G.G.M., Miley G.K. and Willis A.G. 1979, A&AS 35, 153
Tyson J.A. 1988, AJ 96, 1
Wieringa M.H. 1991, Ph.D. Thesis, Leiden University
Wieringa M.H., Katgert P. (1991), A&A 248, L31
Windhorst R.A. 1984, Ph.D. Thesis, Leiden University
Windhorst R.A, Dressler A., Koo D.C. 1987, IAU symp. 124, Observational Cosmology G. Burbidge, L.Z. Fang Eds. (Reidel, Dordrecht), p 573

TABLE 1. *Radio and optical data for the faint USS sources with deep CCD images.*

Name	α_{1950}				δ_{1950}				pos.	S_{92}		S_{49}		S_{20}		α		structure		R	Notes	
	h	m	s	s	°	′	″	″	code	mJy		mJy		mJy				ψ(″)	ϕ(°)	mag.	rad.	opt.
0636+4594	06	36	30.22	±.04	45	56	41.9	±0.4	20C	81	±3	38	±3	14.1	±0.7	1.2	E	12	40		+	−*
0636+4599	06	36	49.74	.03	45	59	49.3	0.3	20A	38	2	19	2	1.6	0.3	1.2 S	E	30	141		+*	−*
	06	36	49.70		45	59	49.5											2	110	21.1		
0639+442	06	39	17.59	.03	44	17	3.2	0.3	20A	34	1	16	3	17.5	0.9	0.4 F	E	20	45		−*	+*S*
	06	39	17.23		44	16	59.1											2	15	22.6		
0642+443	06	42	54.68	.14	44	19	14.2	1.5	50	34	1	14	1			1.4	E	16	89		+	?*
0644+432	06	44	26.04	.03	43	13	6.8	0.4	20C	231	8	88	5	25.2	1.3	1.5	C	0			+	+
	06	44	26.00		43	13	5.6											3	34	23.0		
0644+437	06	44	55.46	.04	43	43	4.3	0.4	20C	78	3	37	2	10.9	0.6	1.3	C	3	147		+	−*
0645+433	06	45	39.88	.03	43	19	19.6	0.4	20C	982	33	461	25	158.1	7.9	1.2	C	5	6		+	−*
0649+446	06	49	45.66	.05	44	38	39.7	0.4	20C	119	4	50	3	11.1	0.6	1.5 S	D	15	28		+*	−*
0653+446	06	53	20.05	.03	44	38	49.6	0.3	20A	102	4	46	4	17.4	0.9	1.2	D	5	29		+*	+*P*
	06	53	20.27		44	38	49.2											5	10	22.8		
0654+448	06	54	49.43	.03	44	48	21.1	0.3	20A	424	15	211	14	68.2	3.4	1.2	C	0			+	+*P*
	06	54	49.64		44	48	21.3											1		23.4		
0822+711	08	22	6.14	.06	71	09	32.9	0.3	20A	32	1	18	1	4.8	0.4	1.1	D	0			−*	+*S*
	08	22	3.42		71	08	57.0											2	79	21.7		
0829+698	08	29	24.84	.07	69	48	41.6	0.4	20C	94	3	46	3	16.2	0.8	1.2	D	16	147		+	?*
0831+457	08	31	54.66	.19	45	43	28.9	1.5	92	173	6	86	6			1.1	E	25	35		+	+*
	08	31	54.61		45	43	26.1											2	121	23.3		
0834+702	08	34	10.54	.06	70	12	52.9	0.3	20A	107	3	51	2	16.6	0.8	1.2	D	3	67		+	+
	08	34	10.82		70	12	51.5											3	21	22.3		
0836+458	08	36	48.79	.04	45	48	5.7	0.4	20C	55	2	24	2	7.7	0.4	1.3	E	11	165		+	−*
0838+450	08	38	46.85	.03	45	04	52.6	0.3	20A	57	2	23	2	9.2	0.5	1.2 F	T	12	170		+*	+
	08	38	46.91		45	04	52.7											2	178	22.5		
0838+456	08	38	52.49	.03	45	41	44.4	0.3	20A	69	2	30	2	15.1	0.8	1.0 F	D	5	153		+*	+*F*
	08	38	52.46		45	41	42.2											2	36	24.0		
0839+457	08	39	16.06	.20	45	44	5.6	1.7	92	41	2	15	2			1.6	E	29	96		+*	−
0839+451	08	39	42.13	.03	45	06	42.7	0.3	20A	80	2	38	2	15.0	0.8	1.1	C	0			+	+*F*
	08	39	42.19		45	06	43.0											2	133	23.7		
0839+693	08	39	50.20	.06	69	23	8.6	0.3	20A	113	4	56	3	19.3	1.0	1.2	C	3	30		+	+*
	08	39	49.92		69	23	9.1											2	153	23.4		
0841+440	08	41	11.30	.03	44	01	10.5	0.3	20A	47	2	20	2	23.0	2.3	0.6 F	E	25	15		−*	?
0841+688	08	41	22.79	.05	68	50	56.8	0.3	20A	93	3	41	3	10.0	0.6	1.4	T	7	140		+*	−
0842+443	08	42	6.07	.05	44	18	26.1	0.5	20C	52	2	19	1	4.5	0.2	1.6	D	7	22		+*	−
0842+450	08	42	42.75	.11	45	02	26.1	1.4	49	28	1	14	1			1.1	E	20	172		−*	?
0845+687	08	45	15.48	.05	68	46	38.8	0.3	20A	70	3	33	4	12.6	0.7	1.2	D	2	99		+	−
0846+718	08	46	7.32	.08	71	49	33.9	0.4	20C	71	3	35	3	12.6	0.6	1.1	C	5	65		+	−*
0846+445	08	46	16.03	.03	44	34	24.9	0.3	20A	286	9	137	7	47.8	2.4	1.2	D	6	57		+*	+*P*
	08	46	16.35		44	34	26.4											6	45	22.4		
0847+451	08	47	4.96	.04	45	06	34.7	0.4	20C	52	2	26	2	9.0	0.5	1.2	C	6	7		+	−
0848+445	08	48	10.12	.03	44	31	11.4	0.4	20C	275	9	133	8	60.2	3.0	1.0 F	C	6	71		+	+*F*
	08	48	10.13		44	31	9.6											5	46	23.3		
0851+717	08	51	20.55	.07	71	44	47.8	0.4	20C	186	6	86	5	29.6	1.5	1.2	D	16	2		+	+*F*
	08	51	20.25		71	44	44.5											2	112	23.8		
1217+664	12	17	27.76	.05	66	28	39.3	0.3	20A	63	2	31	2	14.9	0.8	1.0 F	D	2	163		+	+*F*
	12	17	27.82		66	28	39.8											4	136	23.9		
1221+669	12	21	7.36	.05	66	55	53.2	0.3	20A	50	2	25	1	9.7	0.6	1.1	T	34	87		+*	+
	12	21	8.48		66	55	57.2											2	52	19.0		
1222+675	12	22	8.05	.05	67	30	40.4	0.3	20A	31	1	13	1	3.6	0.3	1.4	T	5	0		+	+*F*
	12	22	7.77		67	30	41.7											3	79	23.8		
1223+672	12	23	50.83	.05	67	12	54.7	0.3	20A	38	1	19	1	9.6	0.6	0.9 F	T	4	127		−	−*
1226+658	12	26	0.80	.09	65	48	44.1	0.3	20A	67	2	31	2	11.7	0.6	1.2	C	7	100		+	−*
1228+652	12	28	21.55	.06	65	16	10.8	0.4	20C	193	7	87	6	31.2	1.6	1.2	C	0			+	−*
1233+656	12	33	15.54	.06	65	39	43.9	0.4	20C	70	3	31	3	9.3	0.5	1.3	D	18	156		+	+*S*
	12	33	16.02		65	39	46.8											3	55	22.6		
1233+655	12	33	46.96	.06	65	31	41.1	0.4	20C	230	8	104	7	33.3	1.7	1.3	C	3	176		+	−*
1233+678	12	33	52.00	.05	67	52	56.5	0.3	20A	31	1	16	1	2.2	0.6	1.4 S	D	6	136		+*	−
1235+655	12	35	15.70	.34	65	33	52.2	1.7	92	85	4	39	5			1.2	E	20	25		+	?*
	12	35	15.70		65	33	53.3											2	168	20.7		
1235+670	12	35	38.24	.38	67	01	21.9	1.8	92	33	1	11	1			1.7	E	20	44		+*	−
1240+682	12	40	57.72	.05	68	17	31.5	0.3	20A	125	5	45	6	30.4	1.5	1.0 F	D	11	73		+*	+
	12	40	57.91		68	17	32.0											2	114	22.9		
1245+667	12	45	37.08	.05	66	42	37.7	0.3	20A	433	11	212	13	105.9	5.3	0.9 F	D	4	6		−	+
	12	45	37.15		66	42	40.2											1	17	23.3		
1246+655	12	46	58.70	.09	65	31	3.9	0.3	20A	36	2	15	1	2.2	0.3	1.4 S	D	4	95		+*	+*S*
	12	46	59.43		65	31	5.8											2	118	21.9		
1247+666	12	47	5.42	.06	66	37	37.8	0.4	20C	88	3	41	3	21.2	1.1	1.0 F	C	3	121		+	+*
	12	47	5.40		66	37	37.5											2	1	20.4		
1302+672	13	02	15.44	.07	67	13	12.8	0.4	20C	51	3	23	1	7.4	0.4	1.3	C	5	99		+	−
1302+676	13	02	37.56	.07	67	40	11.3	0.4	20C	68	7	30	2	8.9	0.5	1.3	D	17	107		+	+*S*
	13	02	37.31		67	40	14.7											3	10	21.5		

Name	α_{1950} h	m	s	s	δ_{1950} °	′	″	″	pos. code	S_{92} mJy		S_{49} mJy		S_{20} mJy		α		structure $\psi(″)$	$\phi(°)$	R mag.	Notes rad.	opt.
1304+668	13	04	13.26	.05	66	54	1.5	0.3	20A	88	3	43	2	16.0	0.8	1.1	E	4	110		+*	+
	13	04	13.32		66	54	2.4											2	109	22.3		
1401+732	14	01	56.25	.09	73	13	39.6	0.4	20C	55	2	22	2	7.7	0.4	1.3 F	C	4	126		+	+*
	14	01	56.23		73	13	39.8											2	1	20.0		
1403+730	14	03	41.77	±.07	73	03	44.3	±0.3	20A	202	±6	100	±3	38.9	±2.0	1.1	D	16	84		+*	+*
	14	03	41.75		73	03	45.0											2	174	23.4		
1412+728	14	12	43.84	.08	72	50	20.5	0.4	20C	163	5	81	3	37.0	1.9	1.0 F	D	11	62		+	+*
	14	12	44.01		72	50	19.0											4	17	23.2		
1413+731	14	13	8.99	.08	73	09	14.9	0.4	20C	235	7	109	3	42.7	2.1	1.2 F	C	3	134		+	−*
1414+743	14	14	19.26	.07	74	22	17.3	0.3	20A	126	4	56	9	22.9	1.1	1.1	D	12	155		+*	−
1415+717	14	15	34.84	.06	71	46	52.0	0.3	20A	43	2	21	3	6.5	0.4	1.2	T	15	33		+	+*
	14	15	35.26		71	46	53.7											3	54	22.8		
1427+726	14	27	33.50	.08	72	39	17.0	0.4	20C	72	3	33	6	13.3	0.7	1.1	C	4	18		+	+
	14	27	33.44		72	39	16.7											5	28	23.2		

Notes to Table 1

0636+4594 close to 17 magn. star (7″ SW), no id.

0636+4599 missing flux + position shift for 20A map, prob. diffuse comp. NW resolved out, SE comp coinc. with opt. object

0639+442 spectrum not steep (prob. resolution effect at 49cm), 3 opt. candidates, most likely one is given

0642+443 no high res. radio data, no id. near 92 or 49 cm pos.

0644+437 stellar object (18.9) at 5″ SE

0645+433 no id. (5*15m total int., $R > 24$)

0649+446 20C: good fit by two gaussian comps(SW: 11″,pa 18; NE: 15″, pa 27), missing flux at 20A; no reliable id. due to radio struct., 2 candidates:19.5 at 064945.29,43832.0, 22.6 at 064945.75, 443843.5

0653+446 missing flux at 20A; prob. identification with aligned, extended object

0654+448 optical obj. extended to SE, cosmic ray 2″W

0822+711 20A shows 2, prob. unrelated, components, both steep (NW:1.6, SE:1.0), but individually below flux cutoff; NW unid., SE id. with 21.7 obj.

0829+698 double + faint unrelated comp. NW at 20A, star (R=13) at 10″SE prevents identification

0831+457 no high res. data; probable faint fuzzy id. close to star (20″SW)

0834+702 id. non stellar

0836+458 no opt. obj. within 10″

0838+450 poss. triple (based on 20C position and hint of S comp. in 20A), spectrum slightly concave (1.4-1.2); id. elongated to S, poss. 2nd obj. 3″ S of core

0838+456 poss. triple; faint, compact id. probable due to radio struct., brighter obj.(19.3) 6″NW on N comp.

0839+4573 not detected at 20 cm; no $R < 23.5$ obj. near low freq. positions

0839+451 opt. object at limit of detection

0839+693 flux missing at 20A; 2nd opt. object (22.3, size 3″ in PA 150) at 3″N (49.987,11.69)

0841+440 no longer in sample (not steep); complex radio structure prevents id.

0841+688 poss. triple with core at 22.5, 58; no id., cosmic near radio pos.

0842+443 pos. shift and C map hint at steep N comp., poss. missing flux at high freq.; no id. near radio peak or poss. midpoint

0842+450 below flux limit

0845+687 20 C map is poor (single snapshot)

0846+718 poss. ext. towards W (pos. shift and C map); no convincing id., faint cand. (23.5) at 4″SE

0846+445 20C: 3 comps, prob. unrelated, 20A: N comp.(brightest) double ; prob id., 2.4″ from midpoint of double

0848+445 spectrum may flatten (1.2-1.0); no conv. id. (poss. very faint ext. obj. 1.8″S of 20C pos.)

0851+717 poss. very faint id. (23.8) near midpoint, pointlike (not cosmic, cosmic SE)

1217+664 faint ext. obj. within 1″, br. double (21.6) 4″ E

1221+669 20A shows double with poss. faint core, off axis, low freq. pos. near strongest comp.; poss. core coinc. with ext. obj., 2nd obj. 4″W

1222+675 20A shows triple; poss. faint id. (23.8) at (07.77, 41.74) on N comp. (08.077, 41.81)

1223+672 no id. within 7″

1226+658 flux missing at 20A; diffuse (22.6, 3″, pa75) obj. at 3.5″E with faint comp. (24) near 20A pos.

1228+652 no id., cosmic ray nearby

1233+656 double at 20C, resolved out at 20A (poss. 2-3sigma det.); poss. id (22.6) at 2.5″NE of 20C c.o.g.

1233+655 id. unlikely due to distance, higher res. radio data needed

1233+678 flux missing at 20A, uneq. double or triple (4″ flux∼2 mJy)

1235+655 only low frequency data, id. probable

1240+682 20C shows double + unrel comp. S; 20A shows two ext. comps (N); fuzzy id.

1245+667 double at 20A, flattens (1.15-0.9); compact id.

1246+655 flux missing at 20A + position shift W, poss. comp. missing to E; R=21.9 obj. likely id. because of radio str. and low freq. pos.

1247+666 fairly bright id. (20.4) in glare of star

1302+676 double at 20C, undet at 20A (hint of W comp); 2 opt cand. N one most probable (fuzzy) pos. offset acceptable based on radio structure (other obj. at 36ˢ.34, 12′.9 with $R = 22.8$)

1304+668 20A shows core with wide tail NW

1401+732 nonstellar, bright id

1403+730 double at 20C and 20A, bridge between comps; 23.4 obj $< 1″$ from c.o.g.

1412+728 likely id. (single 15m exposure, br. star NE)

1413+731 between 2 stars, limit $R > 23$

1414+743 close double + prob. unrel. comp. SE at 20A; no id near double

1415+717 id close to central comp. (2 other obj. SE and SW)

TABLE 2. *Radio data for the faint USS sources without deep CCD images.*

Name	α_{1950} h	m	s	s	δ_{1950} °	′	″	″	pos. code	S_{92} mJy		S_{49} mJy		S_{20} mJy		α		structure ψ(″)	ϕ(°)
0633+455	06	33	13.83	±.03	45	31	26.5	±0.3	20A	43	±4	17	±4	9.9	±0.5	1.0 F	C	15	130
0633+451	06	33	35.13	.03	45	07	4.4	0.3	20A	39	3	19	4	6.3	0.4	1.2	C	0	
0648+444	06	48	9.58	.03	44	27	27.8	0.3	20A	43	2	21	2	4.3	0.3	1.5 S	C	7	135
0650+460	06	50	55.45	.03	46	04	50.1	0.3	20A	31	2	15	1	2.3	0.2	1.7 S	C	5	35
0827+692	08	27	44.87	.07	69	12	45.3	0.4	20C	60	2	30	2	12.4	0.6	1.1	C	3	108
0828+702	08	28	39.72	.06	70	12	43.5	0.3	20A	34	1	17	1	7.7	0.4	1.0	D	10	50
0830+698	08	30	5.43	.06	69	48	51.4	0.3	20A	32	1	14	1	6.9	0.6	1.1 F	C	6	25
0830+689	08	30	32.26	.05	68	54	20.4	0.3	20A	43	2	12	1	2.5	0.2	1.9	C	1	95
0837+459	08	37	48.41	.03	45	57	56.5	0.3	20A	44	2	19	2	8.8	0.5	1.1 F	D	12	120
0839+705	08	39	2.53	.06	70	35	32.4	0.3	20A	50	2	21	1	5.0	0.5	1.5	C	0	
0839+695	08	39	54.06	.06	69	34	45.5	0.3	20A	38	1	20	1	4.7	0.6	1.3 S	C	0	
0840+455	08	40	2.50	.03	45	34	16.5	0.3	20A	37	1	12	2	5.2	0.4	1.3 F	C	0	
0848+694	08	48	19.27	.06	69	29	38.4	0.3	20A	30	1	12	2	5.3	0.3	1.2	C	2	160
0855+7047	08	55	27.50	.07	70	28	39.4	0.4	20C	100	3	47	3	20.4	1.0	1.1	C	10	69
0855+7044	08	55	44.70	.07	70	26	52.1	0.4	20C	79	3	40	3	16.4	1.0	1.0	C	17	131
1219+654	12	19	59.47	.06	65	26	56.7	0.4	20C	133	5	36	5	12.0	0.7	1.6 F	E	22	44
1220+663	12	20	26.28	.05	66	22	16.2	0.3	20A	50	2	25	2	9.4	0.6	1.1	T	6	104
1230+675	12	30	0.05	.05	67	32	4.2	0.3	20A	46	2	21	1	10.7	0.6	1.0 F	C	4	20
1232+667	12	32	42.04	.05	66	42	15.1	0.3	20A	40	2	18	1	3.3	0.4	1.5 S	D	21	64
1256+647	12	56	11.32	.05	64	46	3.0	0.3	20A	48	2	26	2	5.8	0.5	1.3 S	C	6	45
1302+661	13	02	54.40	.15	66	06	59.7	0.6	20A	41	2	18	2	5.3	0.6	1.3	C	5	40
1309+666	13	09	43.52	.05	66	41	45.6	0.3	20A	52	3	25	2	7.6	0.7	1.2	D	6	65
1311+664	13	11	14.73	.08	66	24	43.4	0.3	20A	34	3	16	2	3.6	0.5	1.4	D	17	70
1412+729	14	12	36.80	.07	72	57	32.2	0.3	20A	30	1	14	3	2.8	0.2	1.6	C	0	
1417+722	14	17	9.74	.08	72	17	29.9	0.4	20C	111	4	48	3	14.9	0.8	1.3	C	6	142
1418+734	14	18	1.41	.08	73	24	55.3	0.4	20C	154	5	76	3	27.2	1.4	1.1	C	12	167

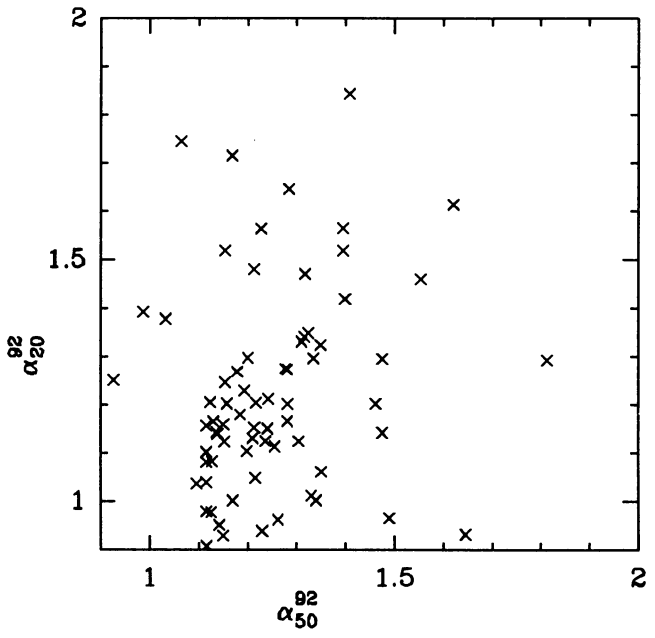

FIGURE 1. The spectral index α_{20}^{92} as determined from the VLA observations at 20 cm, against the selection spectral index α_{49}^{92}.

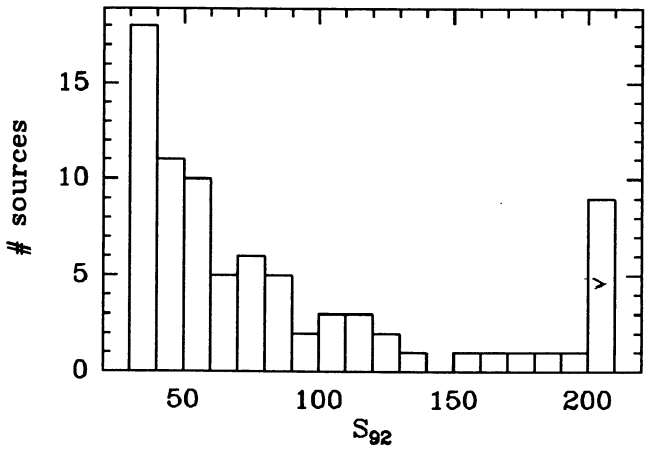

FIGURE 2. Histogram of the 327 MHz (92cm) flux densities of the sources in the USS sample. The highest bin includes all sources with $S_{92} > 200$ mJy.

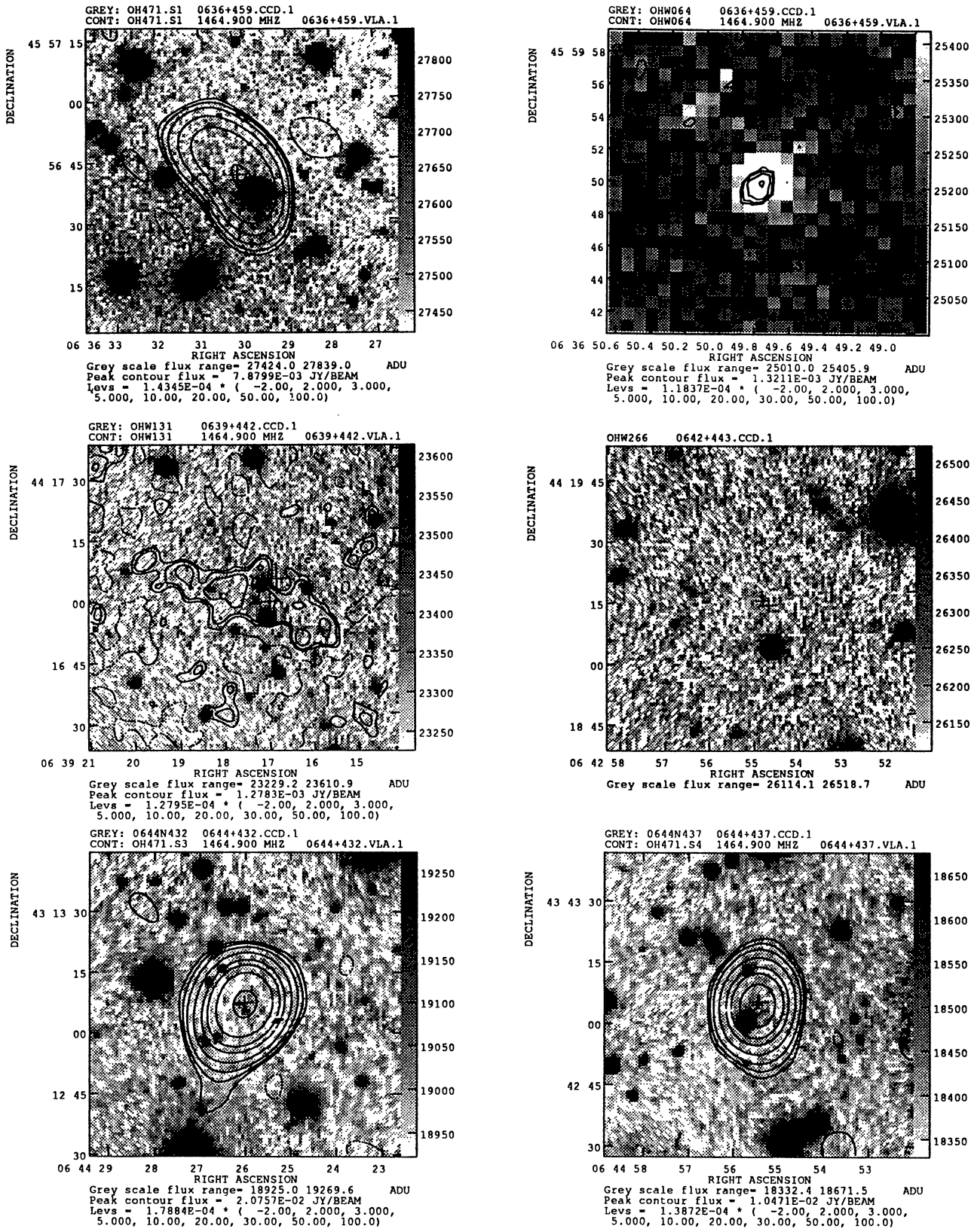

FIGURE 3. Overlay plots of the CCD-images and the VLA radio maps. The grey scales of the optical images are confined to a narrow region around the median (-1σ to $+3\sigma$) to show even the faintest objects. The resolution of the radio maps is either $\sim 1.2''$, $2''$ or $4''$ for the A-array data and $\sim 12''$ for the C-array data. The scale of the plots varies in three steps. The low frequency (327 and 608 MHz) center-of-mass positions are indicated with crosses, the size of the crosses equals the estimated position errors. For a few images only low frequency data are available

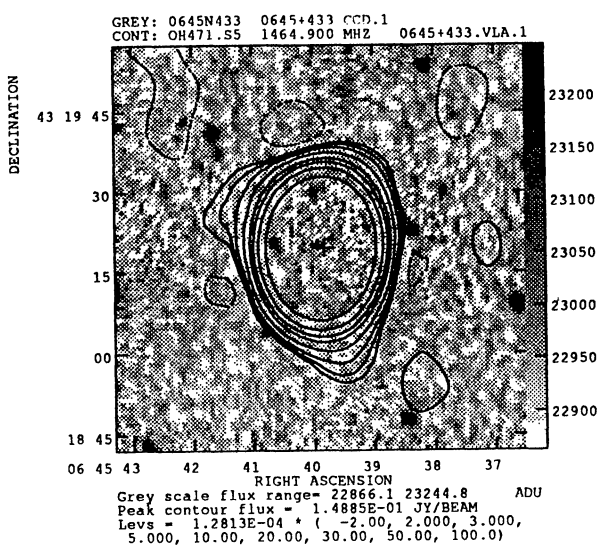

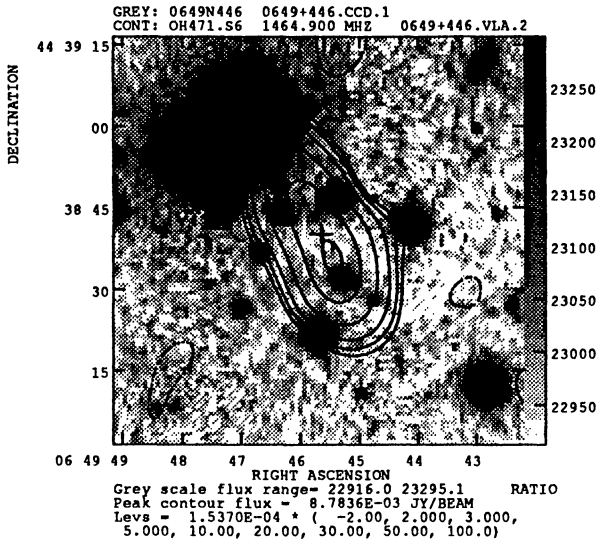

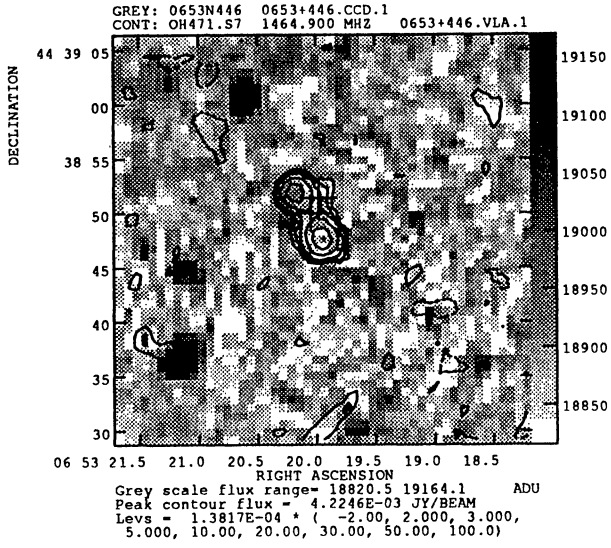

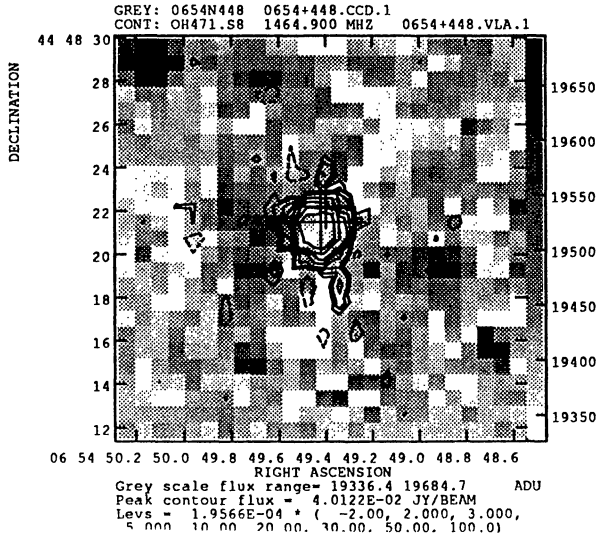

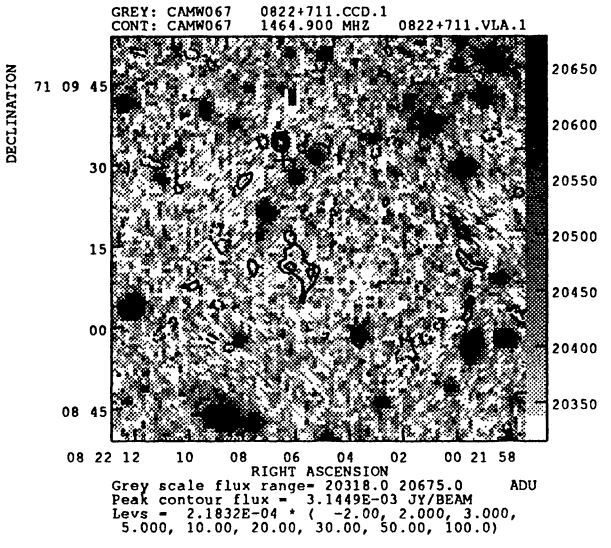

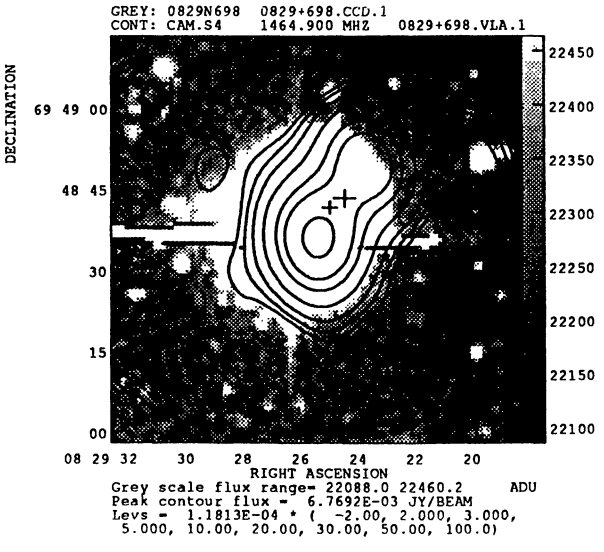

FIGURE 3. *(continued)*

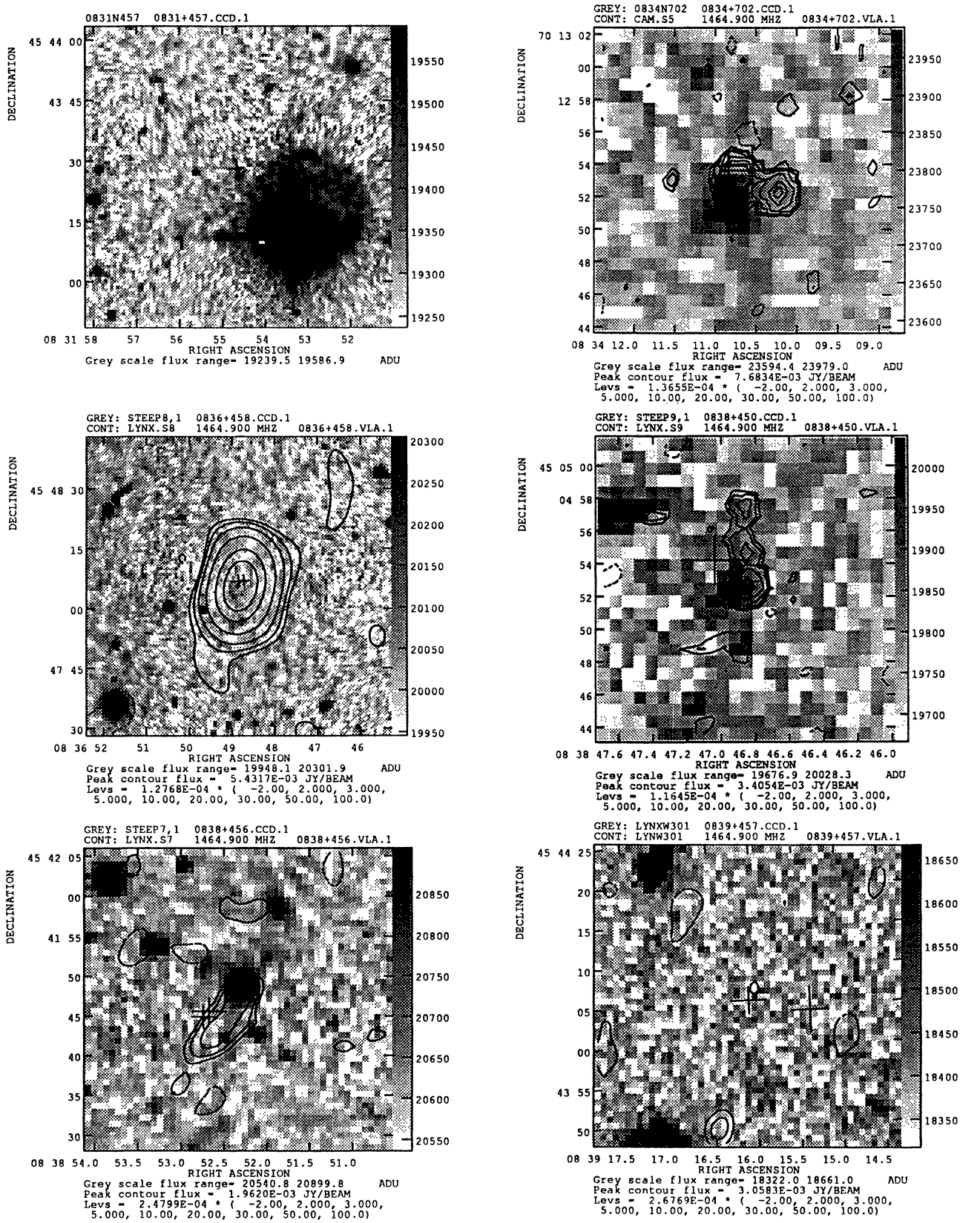

FIGURE 3. *(continued)*

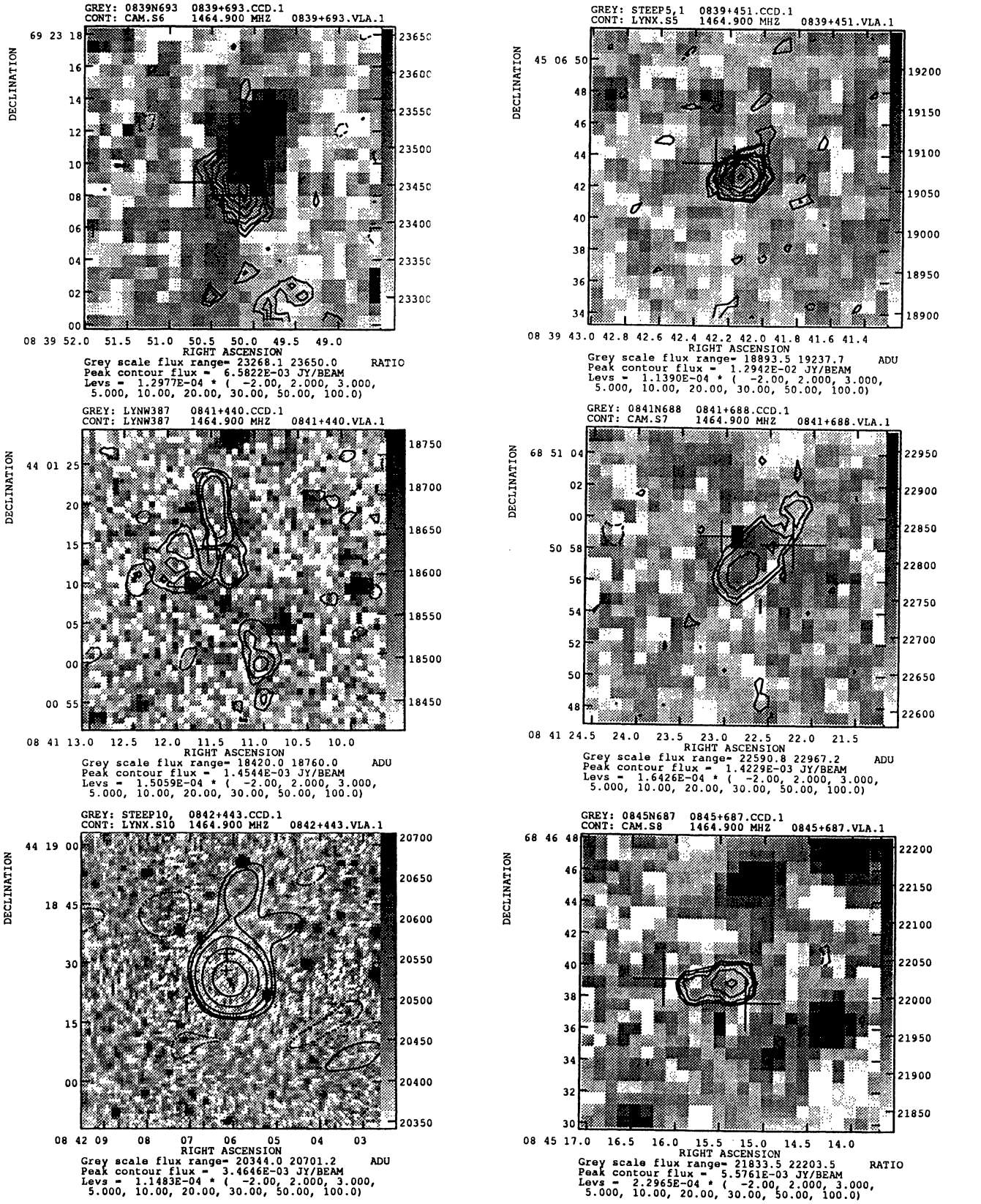

FIGURE 3. *(continued)*

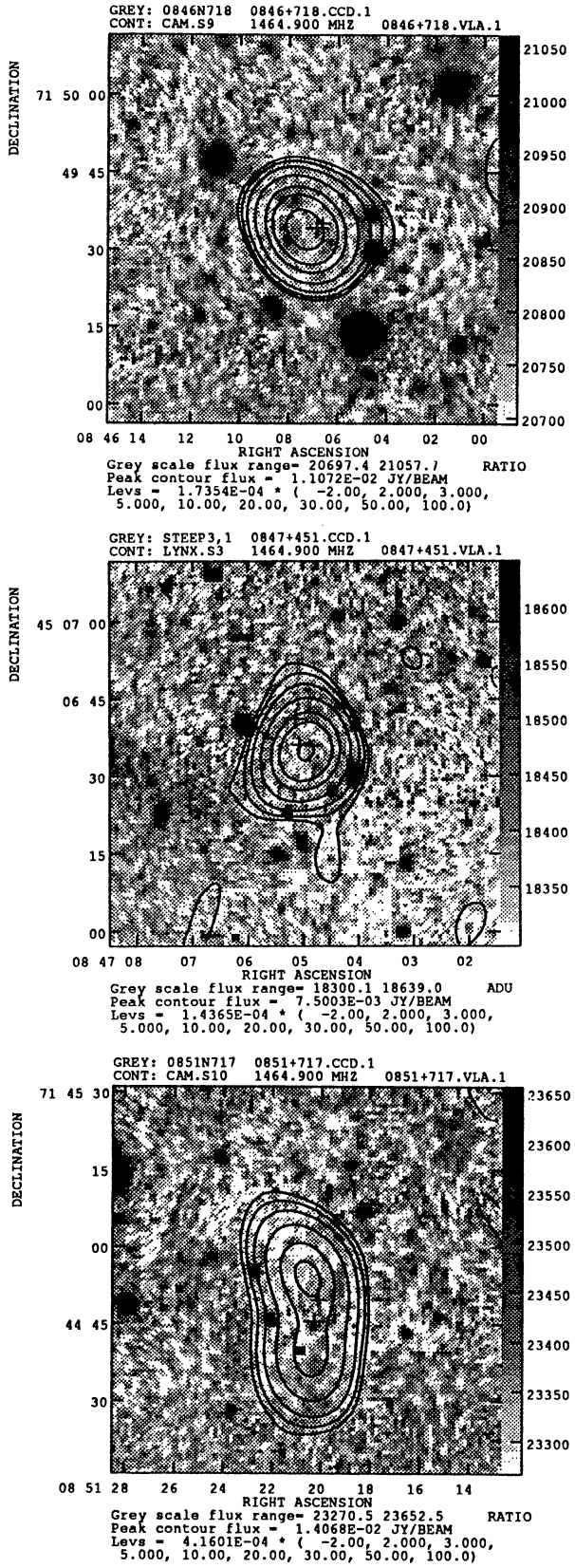

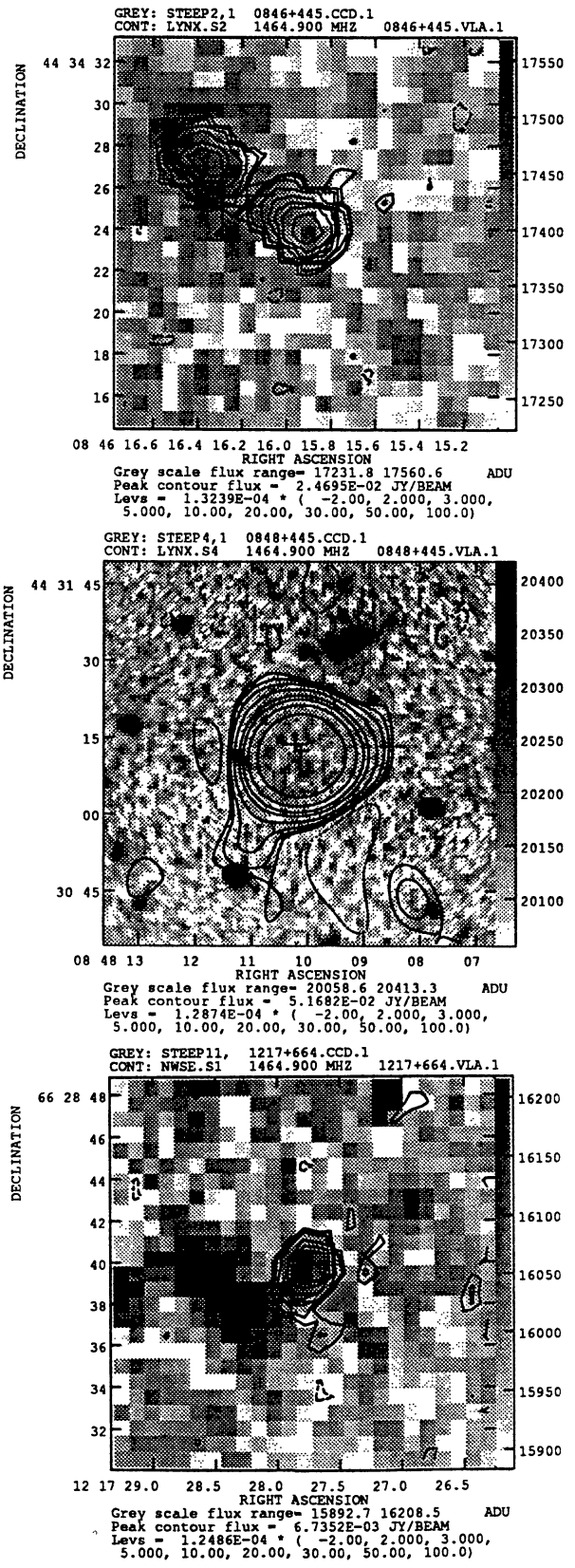

FIGURE 3. *(continued)*

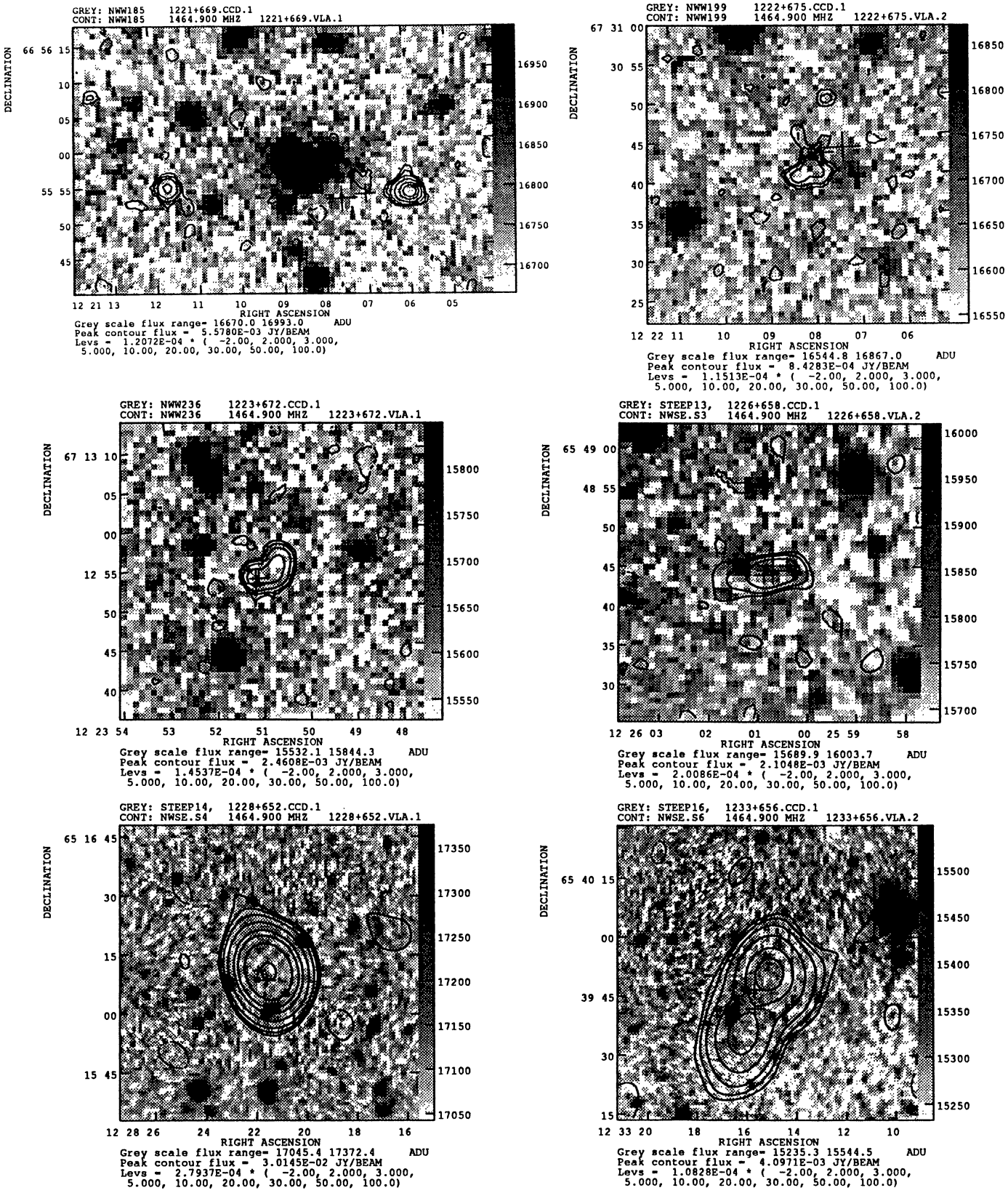

FIGURE 3. *(continued)*

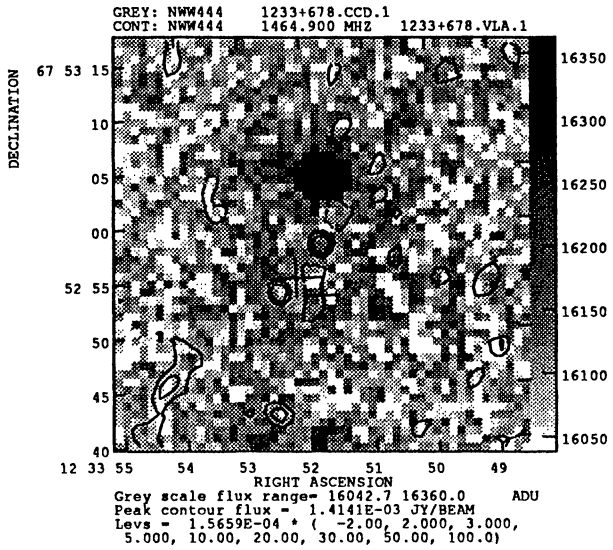

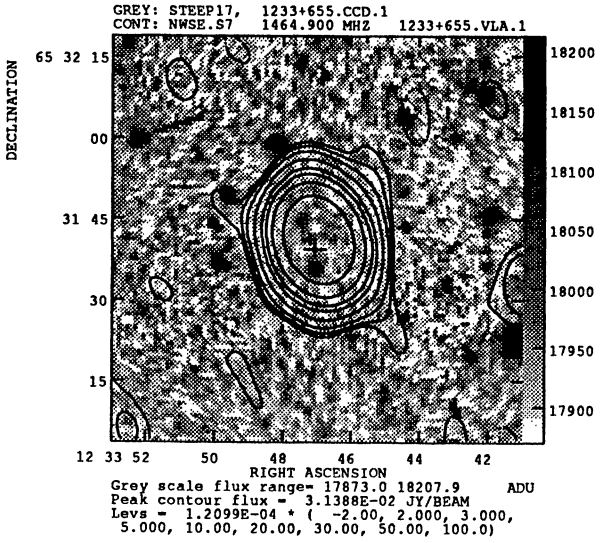

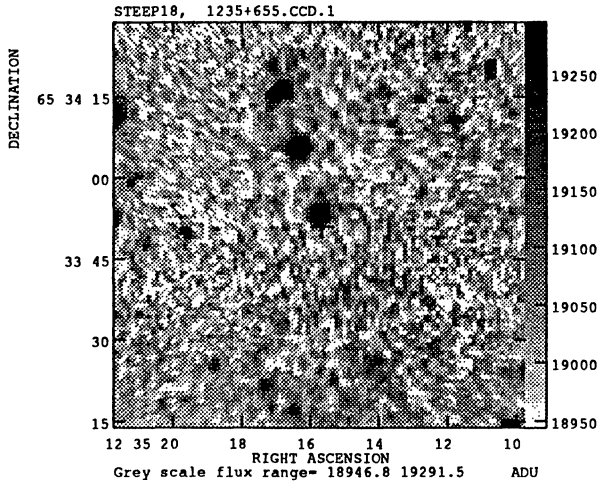

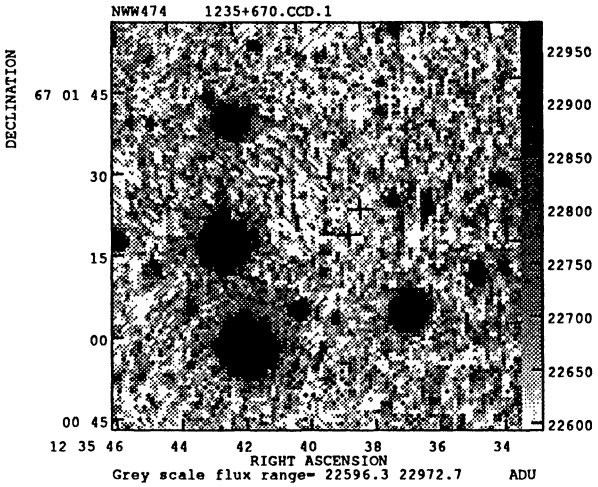

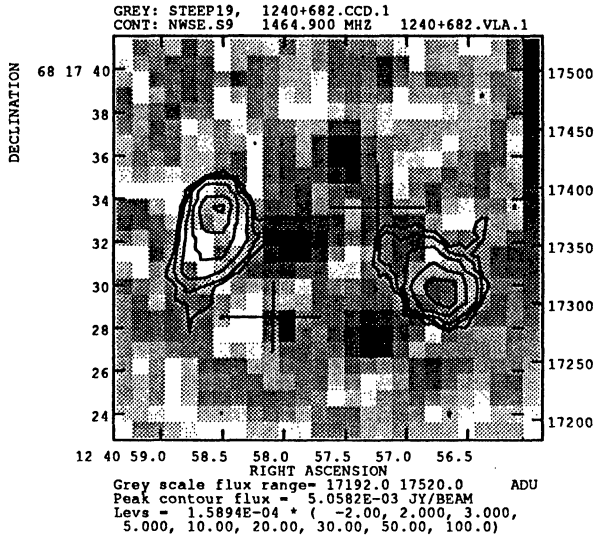

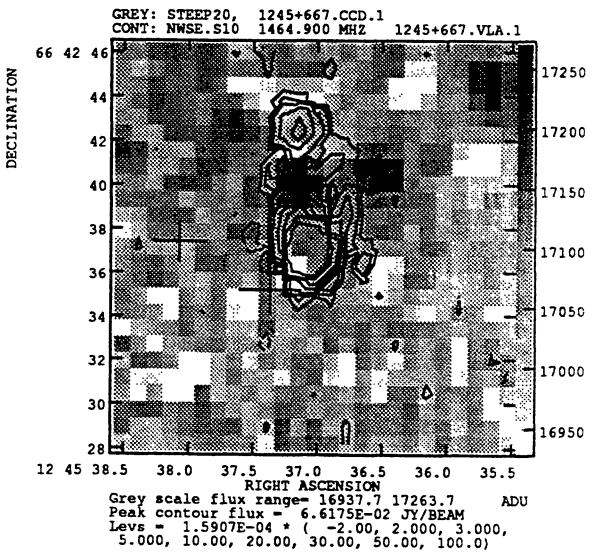

FIGURE 3. *(continued)*

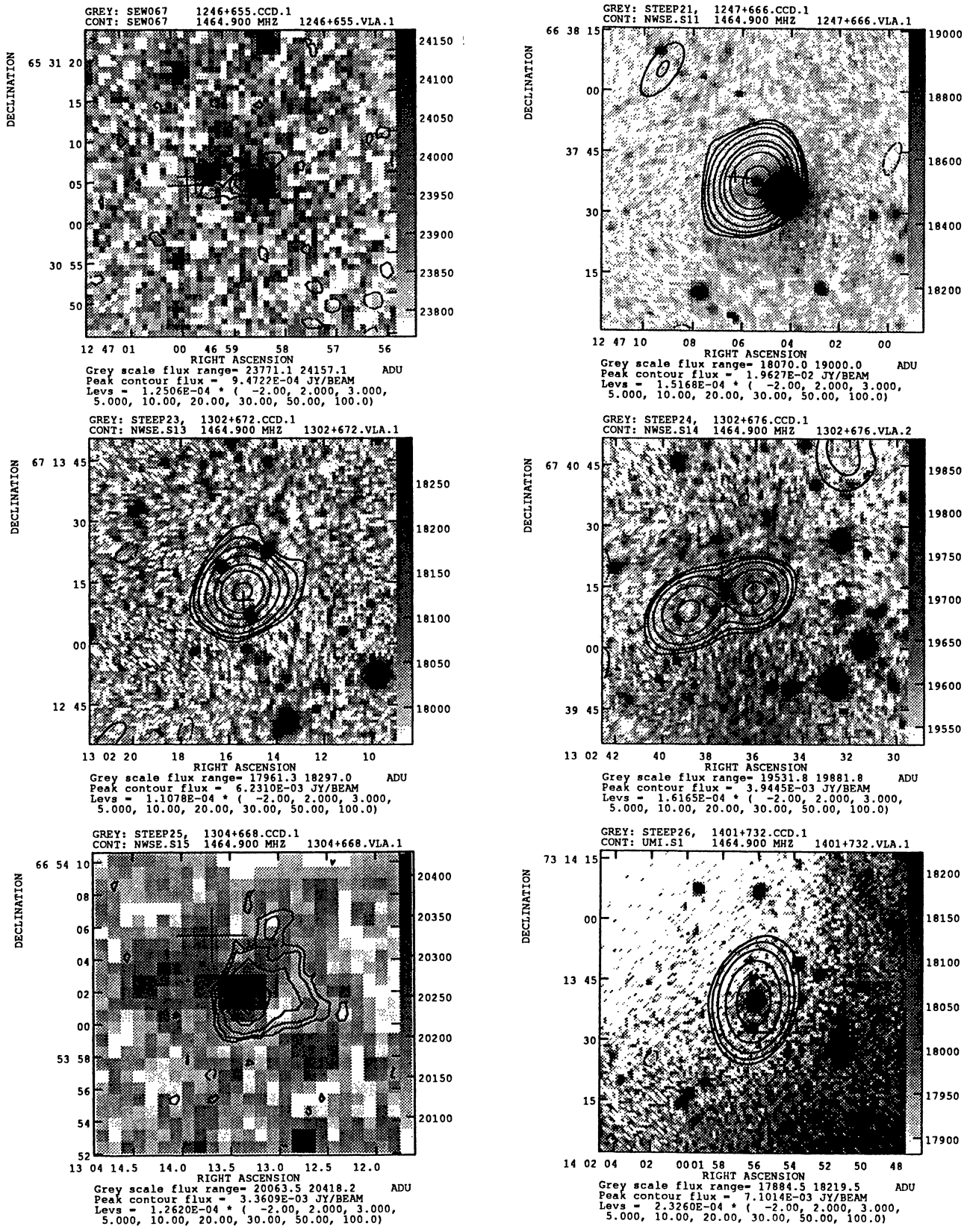

FIGURE 3. *(continued)*

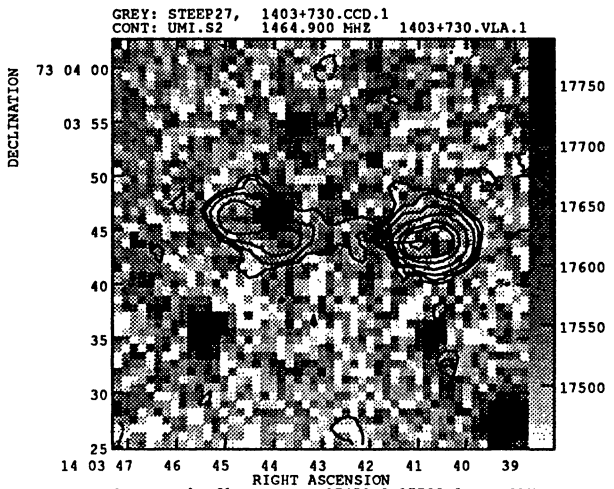

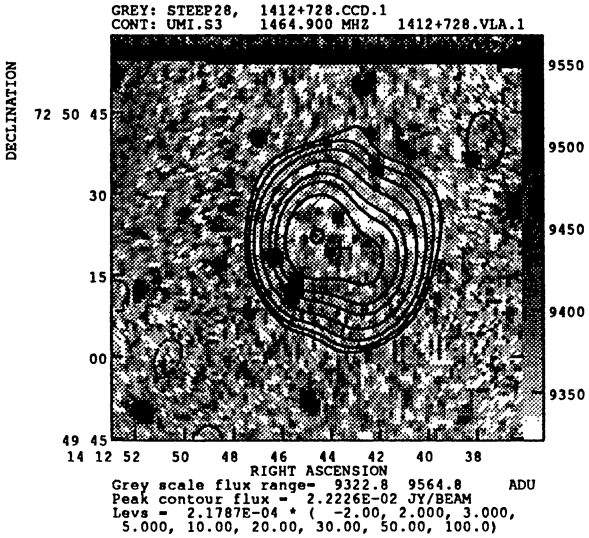

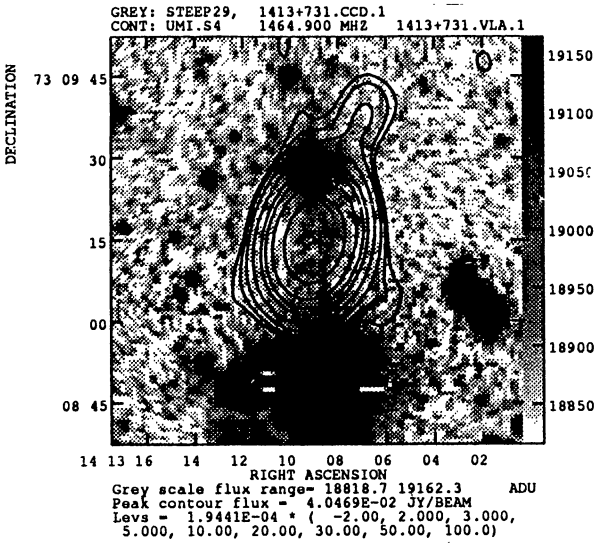

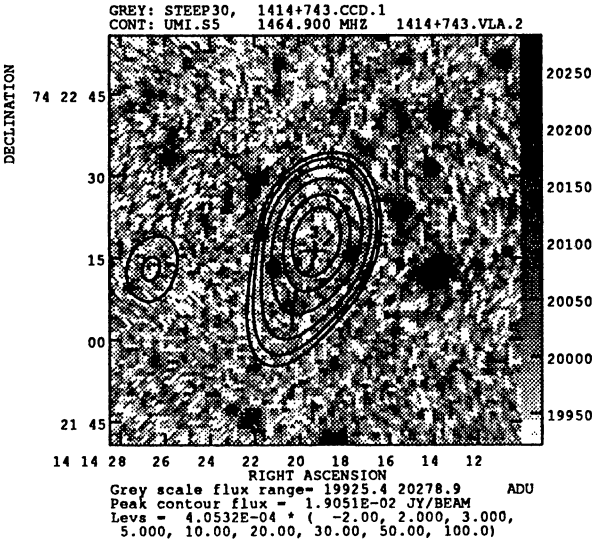

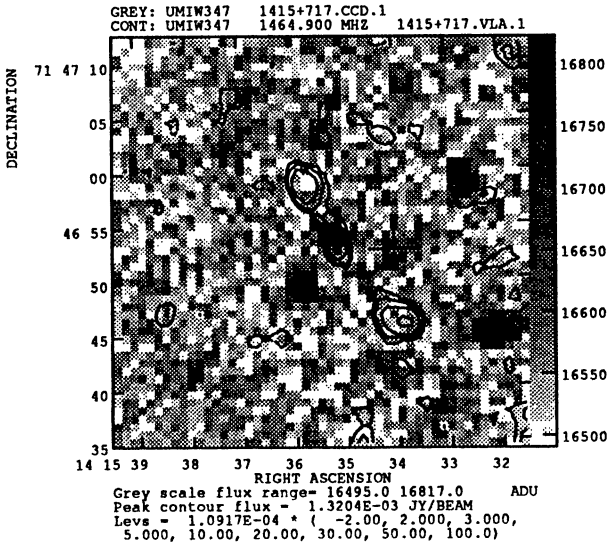

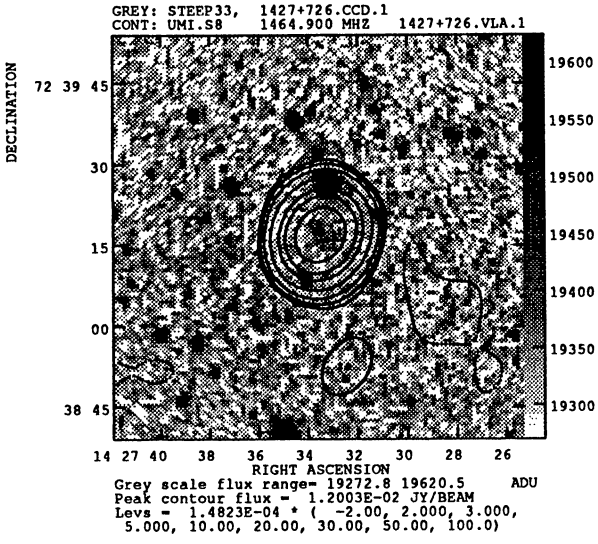

FIGURE 3. *(continued)*

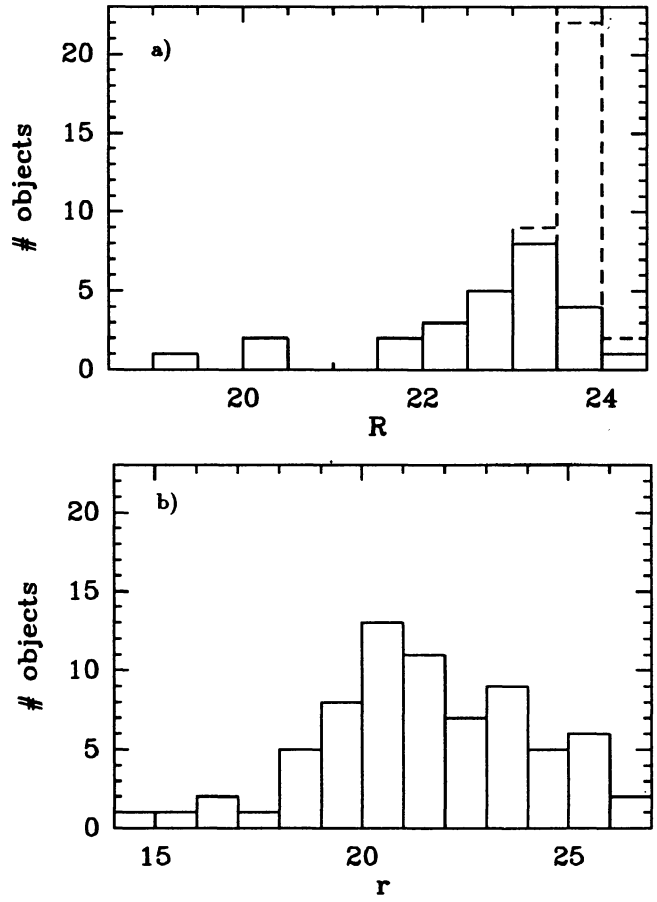

FIGURE 4. a) The R-magnitude distribution of the identified sources. The dashed parts indicate lower limits of R for unidentified sources. b) The magnitude distribution of a 100% identified radio sample of Windhorst *et al.* (1987).

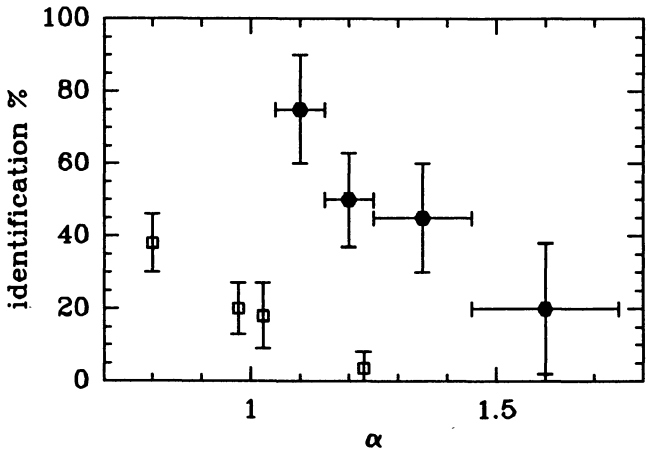

FIGURE 5. The identification fraction against spectral index. The horizontal bars indicate the range of spectral indices included in each point. The open squares represent the data of Tielens *et al.* (1979) for the 4C-sample.

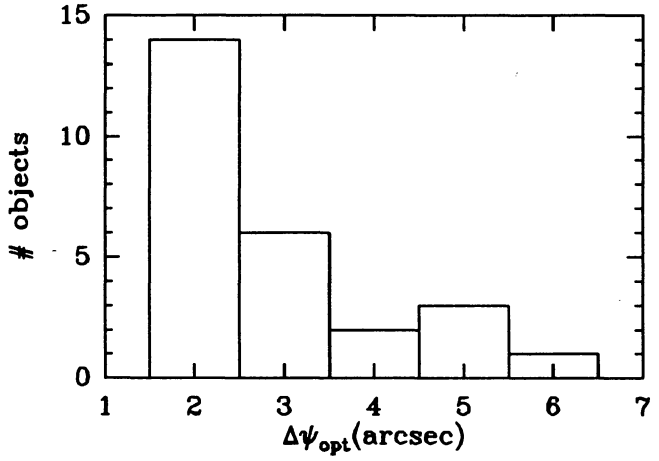

FIGURE 6. The optical size histogram for the identified sources.

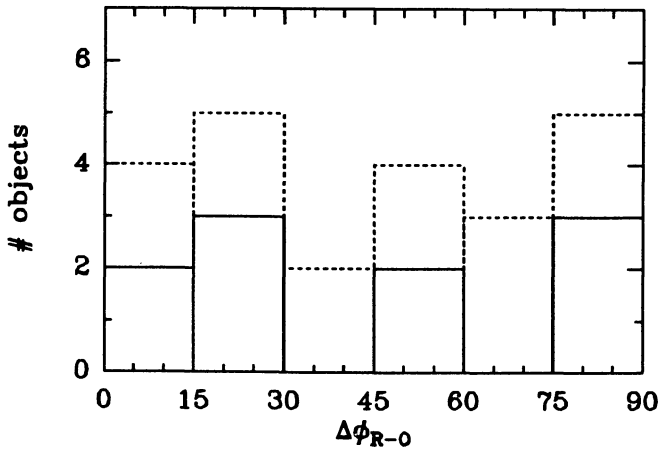

FIGURE 7. Histogram of the radio-optical position angle differences for the objects with radio and optical size $\geq 3''$ (full drawn line) and size $\geq 1''$ (dotted line).